The Canadian Mineralogist
Vol. 32, pp. 919-933 (1994)

MINERAL RECOGNITION IN DIGITAL IMAGES OF ROCKS: A NEW APPROACH USING MULTICHANNEL CLASSIFICATION

PATRICK LAUNEAU* AND ALEXANDER R. CRUDEN

Department of Geology, Erindale College, University of Toronto, Mississauga, Ontario L5L 1C6

JEAN-LUC BOUCHEZ

Laboratoire de Pétrophysique et Tectonique, Université Paul Sabatier, 38, rue de Trente-Six-Ponts, 31400 Toulouse Cedex, France

ABSTRACT

Digital image-analysis is used for counting (modal analysis) and measuring grains (texture and fabric analysis). Traditionally, minerals are visually recognized and manually outlined prior to digitizing and subsequent analysis. This limitation can be overcome by using multichannel methods of classification, in which the minerals in multichannel digital images are accurately recognized on the basis of their unique spectral or elemental signatures, established by a training stage prior to classification. The technique is applied here for the modal analysis of three-color, electro-optical images digitized using CCD video cameras and scanners, and multi-elemental X-ray maps acquired with an electron microprobe. In all three case studies of the analysis of plutonic igneous rocks, the resulting mineral modes are sufficiently precise to identify significant compositional heterogeneities between groups of samples and, in the case of X-ray element maps, to quantify the degree and type of alteration.

Keywords: digital images, multichannel classification, electro-optical devices, electron microprobe, X-ray element maps, modal analysis.

SOMMAIRE

L'analyse d'images numériques de roches est utilisée pour calculer des surfaces (analyse modale), compter des grains (granulométrie), mesurer leur forme et leur orientation (analyse de textures et de fabriques). Habituellement, les minéraux doivent être au préalable identifiés et dessinés par l'opérateur avant d'être numérisés pour l'analyse. A cette identification longue et laborieuse, il est préférable d'utiliser des classifications multispectrales semi-automatiques, rapides et objectives. Un minéral est alors identifié par une signature spectrale spécifique obtenue lors d'un échantillonnage de l'image précédant la classification. La technique est appliquée ici à des images couleur (rouge, vert, bleu) montrant la distribution modale des minéraux, numérisées par caméra CCD et scanner, et aussi à des images de distribution d'éléments, telle que révélée par rayons X, et obtenues par microsonde électronique. Dans les trois exemples de roches ignées et plutoniques, les déterminations de mode sont suffisamment précises pour identifier des hétérogénéités significatives du mode d'un groupe d'échantillons à l'autre. Dans le cas des cartes de rayons X, on peut même quantifier le degré et le type de l'altération.

Mots-clés: images numériques, classification multispectrale, détecteurs électro-optiques, microsonde électronique, carte de rayons X, analyse modale.

INTRODUCTION

In the classical approach to characterize the mode, texture and fabric of a rock, the minerals must be visually recognized prior to point counting (modal analysis) or the preparation of a grain-boundary map (texture and fabric analysis). Point counting is tedious, and petrologists commonly prefer to a use whole-rock chemical composition for normative classification. Likewise, the use of indirect methods (anisotropy of magnetic susceptibility, X-ray texture goniometry, *etc.*) is common in structural petrology for fabric analysis. However, there are many circumstances in which direct analyses of mode and fabric are desirable.

Image analysis has long been recognized as potentially useful to count and measure grains in rocks.

* Present address: UFR des Sciences et des Techniques, Laboratoire de Pétrologie Structurale, Université de Nantes, 2, rue de la Houssinière, 44072 Nantes Cedex 03, France.

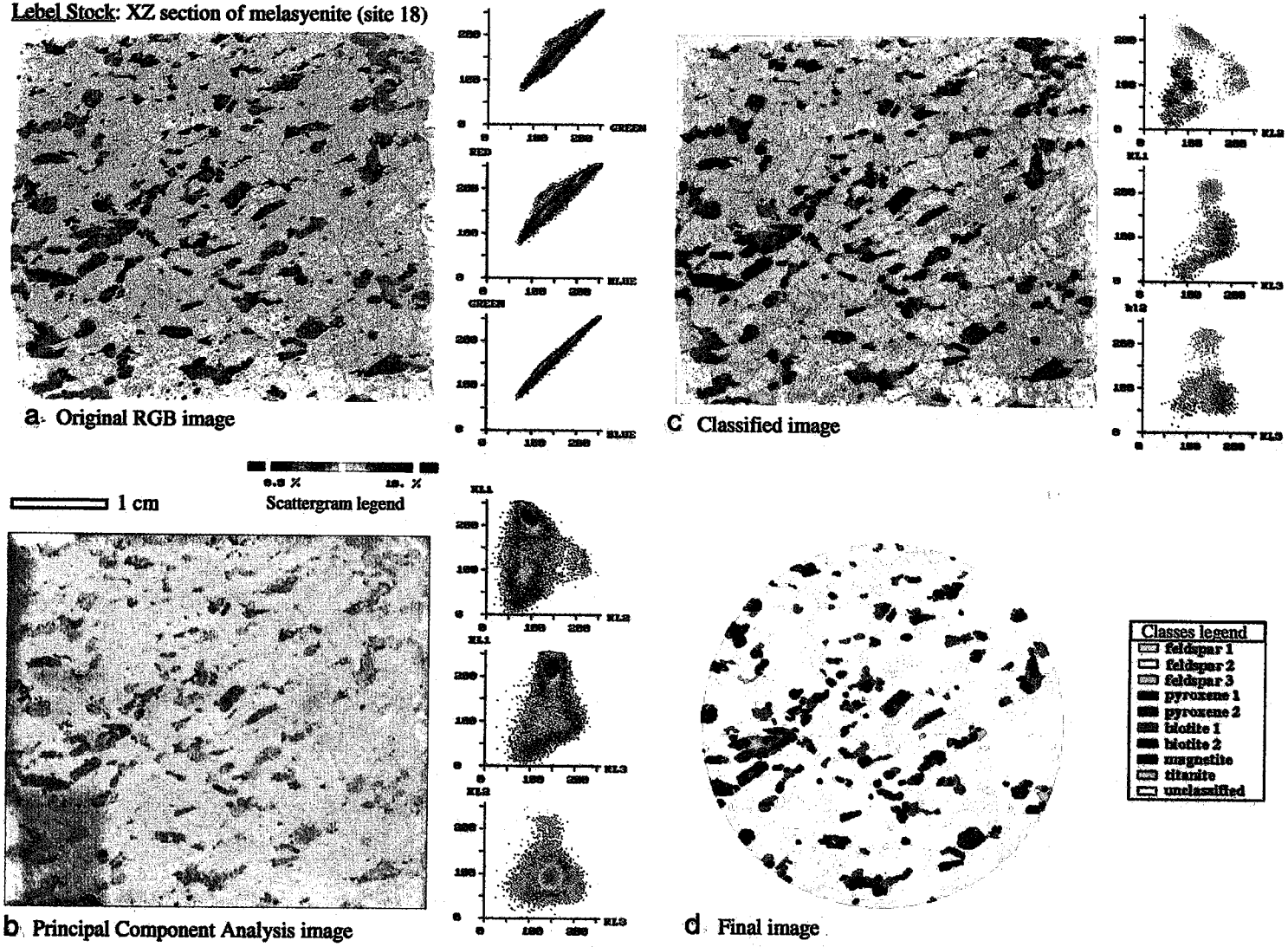
Lebel Stock: XZ section of melasyenite (site 18)
a Original RGB image
c Classified image
1 cm
Scattergram legend
b Principal Component Analysis image
d Final image
Classes legend
feldspar 1
feldspar 2
feldspar 3
pyroxene 1
pyroxene 2
biotite 1
biotite 2
magnetite
titanite
unclassified

However, one of the main problems encountered is the recognition and separation of minerals in digital images. Traditionally, the operator has identified grains visually and outlined grain boundaries manually (Fabbri 1984). Here, we describe a method for semi-automatic identification of minerals in multichannel digital images of planar sections of rocks. The technique is based on multispectral classification, which is used extensively in remote sensing (Lillesand & Kiefer 1987, Campbell 1987), and can be applied to all types of multichannel digital images. We illustrate the use of classified images for modal analysis with three case studies: (1) analysis of thin sections of syenites from the Lebel Stock, Abitibi Greenstone Belt, northern Ontario, digitized using a flat-bed scanner, (2) analysis of stained slabs of granitoid rocks from the Mont-Louis – Andorra pluton, French Pyrénées, digitized with a video camera, and (3) analysis of major-element X-ray maps of a granophyre from the Sudbury Igneous Complex, Ontario, generated with an electron microprobe.

Digital Images

A digital image is an array of numbers (pixels) depicting the spatial distribution of a measurable parameter. The relative intensity of each pixel is expressed as a grey level, which ranges from 0 (black) to 255 (white). In geology, such images are conventionally acquired (digitized) using electro-optical devices, such as CCD video cameras and flat-bed scanners (Appendix), or by X-ray element mapping with an electron microprobe, or from scanning electron microscopes. If more than one parameter is measured, then the image is referred to as a *multichannel* (or *multispectral*) image.

Image processing

Digital image processing (Jähne 1991, Russ 1992) is used for enhancement of the image and extraction of information (Lillesand & Kiefer 1987). Most digital images must be filtered because of inherent noise produced during signal generation and digitization. For most images discussed here, we have found it sufficient to apply a blank-image correction, to minimize the effects of lighting or variations in thickness of thin sections, followed by sequential application of a low-pass filter (Pratt 1978) to reduce noise, and a final sharpening filter (Laplacian of the image added to the image; Jourlin 1987, Russ 1992) to eliminate the blur introduced previously (Appendix). Any processing of the image at this stage must be global and linear in order to preserve the relations among pixels and to safeguard their content of information.

In multichannel digital imagery, the channels are commonly correlated. For example, pixel values in all three channels of the RGB (red, greeen, blue) image of Figure 1a show a strong linear relationship. In such cases, it is useful to decorrelate the information carried by each channel using Principal Component Analysis (PCA; Appendix). The objective of PCA is to determine a new, orthogonal set of axes by the Karhunen–Loeve (KL) transformation, which recognizes the maximum variance in the multichannel data. Projection of the data onto these axes results in as many new KL channels as there are input channels; thus the original R,G and B channels (Fig. 1a) are transformed into KL1, KL2 and KL3 (Fig. 1b), which are now decorrelated.

Significance of pixels

Pixels record information from a finite area, leading to the occurrence of "pure" and "mixed" pixels (Fig. 2a). Consider a rock consisting of four phases, in which the fourth phase is an alteration product of phase 3. Pure pixels are recorded only from inclusion-free phases (1 and 2) away from the grain boundaries (Fig. 2a). When pixels record information from more than one phase, they represent an average of the information (*i.e.*, they are mixed). In the example, the digital image is incapable of resolving phases 3 and 4. However, a distinct object, the characteristics of which are an average of these two phases, is detectable (Fig. 2b).

Pixel size and spatial resolution are strongly dependent on the digitizing device. CCD video cameras offer the greatest range of resolutions between 1 mm and 50 μm; flat-bed scanners have typical pixel sizes of 80 to 40 μm (300 to 600 DPI). The resolution of X-ray maps is given by the width of the electron beam, which can vary from 50 μm (defocused beam) to 1 μm (focused). The choice of device is therefore dictated by the nature of the sample and technique to be used.

FIG. 1. Four stages in the multispectral classification of a thin section of alkali feldspar melasyenite from the Lebel Stock. (a) Original RGB image digitized with a flat-bed scanner, after improvement with a denoising filter. Scattergrams next to the image show the relative RGB contents of each pixel. (b) False-color composite image of the KL channels (KL1: Red, KL2: Green, and KL3: Blue) and corresponding scattergrams after decorrelation of the original RGB channels by Principal Components Analysis. (c) Resulting image after training and classification (see text). Scattergrams show how each subclass is defined in KL channel space. (d) Final image after grouping of subclasses and postclassification smoothing.

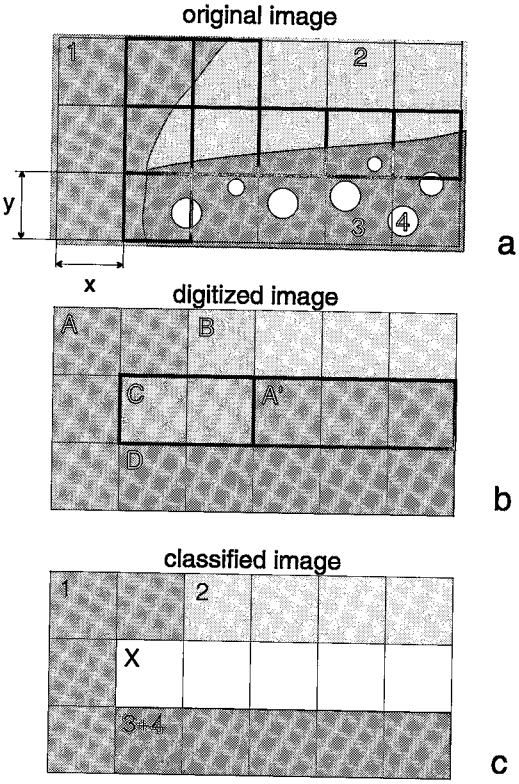

FIG. 2. Problems associated with digitization and classification of an image with pixels of finite size (x, y). The original image (a) contains four phases. Mixed pixels typically occur at grain boundaries (bold pixels), or where inclusions are smaller than the pixel size (*e.g.*, inclusions of phase 4 in phase 3). In the digitized image (b), four classes of pixels are identified and classified on the basis of their grey levels, but some pixels have been misclassified at this stage (bold pixels). The classification was carried out as follows: class A: pixels classified as phase 1, class A′: pixels misclassified as phase 1, class B: pixels classified as phase 2, class C: unclassified pixels, class D: mixed pixels classified as phases 3 + 4. In the classified image (c), classes A, B and D have been replaced by a code (grey level) identifying the respective phases (1, 2 and 3 + 4). Classes A′ and C have been deleted and replaced by a code, X, representing all unclassified pixels, by application of a smoothing filter (see text).

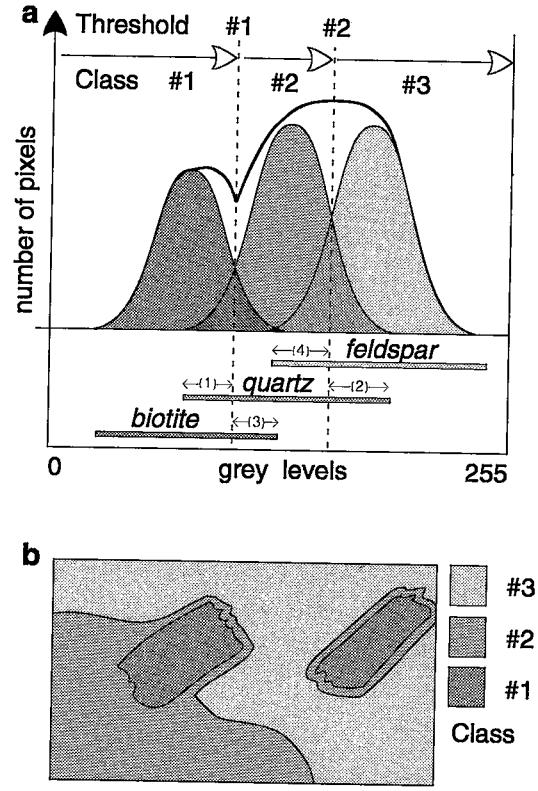

FIG. 3. Problems associated with thresholding a single-channel digital image. On the image histogram (a), the total count of grey-level values (heavy curve) is made up of the individual grey-level ranges of biotite, quartz and feldspar. Best-fit limits or thresholds between the mineral phases (dashed lines) can be defined in order to classify all the pixels in the image (b). Because of the overlap between the grey-level ranges of the minerals, this thresholding process will result in misclassification of some pixels, particularly at grain boundaries.

Mineral recognition in digital images

Mineral recognition in single-channel (monochrome or monoelement) digital images must be done on the basis of relative intensity of light or grey-level alone. However, such images usually display significant overlaps in grey-level ranges corresponding to the different minerals (Fig. 3a), and unless the image is strongly bimodal, any attempt to separate phases by thresholding the image histogram (Fig. 3a) will result in a significant amount of misidentification (Fig. 3b). This problem can be alleviated by using a three-channel color image, because with a coding of 8 bits per pixel in each channel, 256^3 potential colors are available for mineral recognition instead of the 256 grey levels of a monochrome image. *This is the rationale for using multichannel classification; minerals can be accurately identified on the basis of their unique signatures in multichannel data* (unique colors or combinations of element concentrations).

Multichannel Classification

The multichannel (or multispectral) technique of classification is well established in the field of remote sensing, where it is used to characterize and map surface materials that are detectable in multispectral satellite and airborne digital data (*e.g.*, Lillesand & Kiefer 1987, Campbell 1987, Gupta 1991). We focus here on its specific application to the characterization of mineral assemblages. A step-by-step description of the various procedures required to accurately identify minerals in a digital image follows, using the analysis of an alkali feldspar syenite as an example (Fig. 1). With the appropriate software (Appendix), the classification of an image usually takes several hours. When a suite of rocks with similar compositions are analyzed, the classification established for the first image can be applied to all subsequent samples, in which case the time spent on each image is substantially reduced.

Training stage

The first step, or "training" stage, of the mineral-recognition procedure involves sampling, in each channel, the characteristic grey-levels of previously identified minerals (Fig. 4a). A mineral *phase* is then defined as a set of pixels that falls within a characteristic range of color or *class* (Fig. 4b). Because of alteration and residual noise, sampling of a number of grains of each mineral is recommended. The number of samples will be determined by the variability of the mineral. In some cases, it is useful to define *subclasses*, in which case both the host mineral and its alteration product(s) are sampled (*viz.*, Fig. 2a). In the syenite example, three subclasses of feldspar, two of biotite, two of pyroxene, one of magnetite and one of titanite were defined (Fig. 1c).

Supervised classification

The second step is a "supervised" classification of all the pixels using the above definitions of mineral phases. The success of the classification strongly depends on how representative the initial sampling of minerals was with respect to the range of colors available in the image. If sampling was insufficient, then a large number of pixels will be misclassified or unclassified.

The "parallelepiped" method is the simplest technique of classification (*e.g.*, Campbell 1987, Jähne

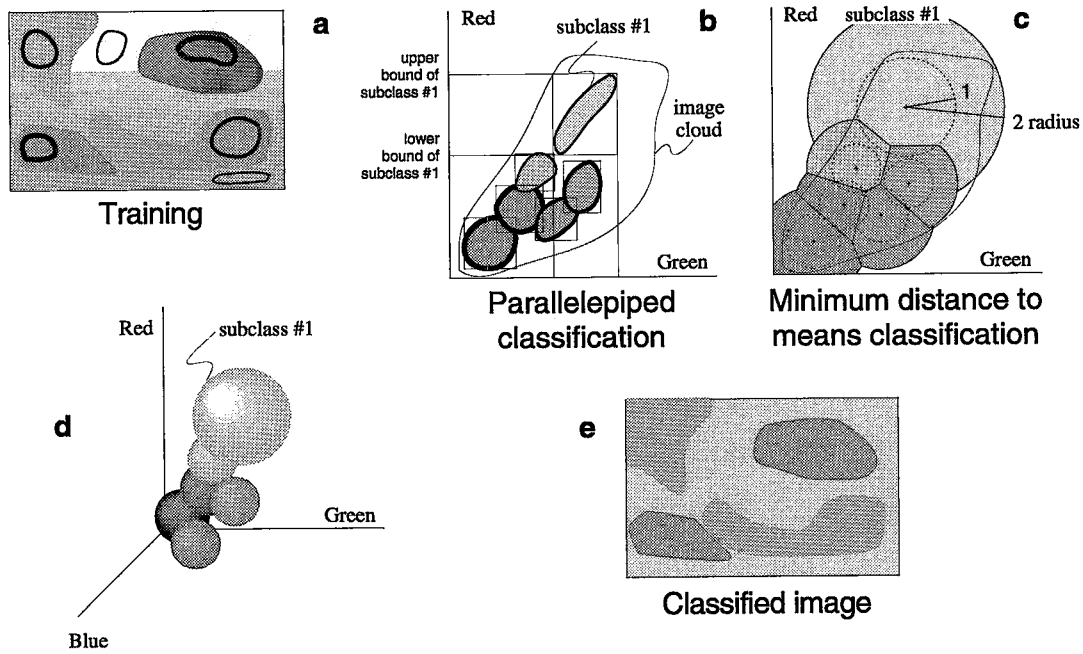

FIG. 4. Stages in the multispectral classification of a three-channel image. During the training stage (a), subclasses are defined and sampled from sampling areas outlined on the raw digital image, and the results are displayed on scattergrams (b). Subclasses, outlined with heavy lines in (b), can be characterized using parallelepipeds (or rectangles in two dimensions), but a "minimum distance to means" classifier (c) results in fewer misclassified and unclassified pixels. In three-channel space (d), subclasses are represented by spheres, and overlaps between classes are smaller than if parallelepipedic boundaries were used. These subclass definitions are then used to classify all pixels in the image (e).

1991). Minimum and maximum bounds of grey-level values for each subclass are determined. A subclass is then defined by a rectangular box (Fig. 4b) in two-channel space and by a parallelepiped in three-channel space. Pixels whose intensity values fall within a given parallelepiped can now be classified, whereas those falling outside or where two parallelepipeds overlap remain unclassified. In practice, the most appropriate limits between classes are chosen after several iterations.

Because of these limitations, we use the "minimum distance to means" or "barycentric" method (Lillesand & Kiefer 1987), in which a class or subclass is defined as a spherical cloud of data. The division between subclasses is chosen on the basis of the distance between the centers of the clouds, and each subclass is characterized by a centroid and a radius (Figs. 4c, d). Because only relatively few pixels are sampled during the training stage, the radius of each subclass is normally doubled for the final classification (solid lines in Fig. 4c). This ensures that the majority of pixels are classified (Fig. 4e). Where two subclasses overlap, their boundary is redrawn at mid-distance from their centers (straight boundaries in Fig. 4c). In the classified image (Fig. 1c), the original color-variations of the principal component image (Fig. 1b) are now concentrated into discrete color-codes corresponding to mineral subclasses and unclassified pixels.

Improving the classified image

Classified data commonly have a salt-and-pepper appearance (Fig. 1c), owing to the large number of subclasses and the presence of misclassified pixels. Regrouping of subclasses produces a substantial visual improvement, but does not eliminate misclassified pixels, which inevitably occur either as isolated pixels or as one-pixel-thick lines between minerals. More generally, grain boundaries look jagged. Both effects can be removed by applying an "edge-smoothing filter" (Launeau *et al.* 1990), which slightly increases the percentage of unclassified pixels, but removes all small within-phase holes, jagged edges, and reduces the number of misclassified pixels at phase boundaries. In our example (Fig. 1d), unclassified pixels now represent 5.7% of the image following this procedure. In classified X-ray maps, misclassified and unclassified pixels are mainly due to noise with a Poisson spatial distribution, occurring as isolated pixels or as strings of pixels within grains. In this case, a statistical smoothing filter, as suggested by Ripley (1988), is useful (Appendix).

APPLICATIONS

Once minerals have been recognized and separated in digital images, many rapid, precise measurements can be made. For example, the intercept technique (Launeau *et al.* 1990) can be used to quantify the anisotropy of individual mineral phases in classified images (Launeau & Bouchez 1992, Cruden & Launeau 1994). Crystal shapes, spatial arrangements and size distributions also can be measured (Cashman 1990). Three case studies, in which different types of image were used for modal analysis, are presented.

Calculation of mode

Modal analysis of a classified image is obtained by dividing the pixel counts for each mineral by the number of classified pixels. Unclassified pixels are thereby redistributed in proportion to the mode of each phase. Because unclassified pixels of electro-optical images are concentrated along grain boundaries, a correction of their redistribution using grain perimeters may be envisaged but does not improve the precision of the mode by more than 1%. In the syenite (Fig. 1), we find: feldspar = 79.9%, biotite + magnetite = 3.6%, pyroxene = 10.5%, titanite = 0.3%, with 5.7% pixels unclassified. The recalculated mode using 94.3% classified pixels is, therefore: 84.7% feldspar, 3.8% biotite + magnetite, 11.1% pyroxene and 0.3% titanite. Differentiation between biotite and magnetite was not possible owing to their similarity in tone and color in the image.

Lebel Stock (flat-bed-scanner images)

The Lebel Stock is a 6-km wide, *ca.* 2673 Ma old syenitic pluton located in the Kirkland Lake area of northern Ontario (Wilkinson *et al.* 1993). Internally, it shows a weak, concentric, transitional zonation from a 100- to 1000-m-wide marginal zone of medium- to coarse-grained alkali feldspar melasyenite to coarse-grained alkali feldspar syenite, which occupies most of the central regions of the intrusion (Cruden & Launeau 1994). Modal analyses of six representative samples within the stock (Fig. 5) were carried out on 4×6 cm polished thin sections, cut parallel to the principal planes of the magnetic fabric ellipsoid of each sample. A three-channel (RGB) digital image of each thin section was made with a color flat-bed scanner with a spatial resolution of 300 DPI (Appendix).

A principal component analysis (PCA) was necessary for mineral identification because of the strong correlation among channels in the images (Fig. 1a). Following classification, modal analysis was done on counting areas *ca.* 15 cm^2 (*ca.* 188 000 pixels). Because of the scale used and the problems of separation discussed above, modes of magnetite and biotite were calculated together.

The percentage of K-feldspar increases from 73% in the melasyenite at the stock margin to 93% in the syenite at the center (Fig. 5b). These modes also indicated a previously unrecognized intermediate facies with 84% K-feldspar. Modes of pyroxene are 22%,

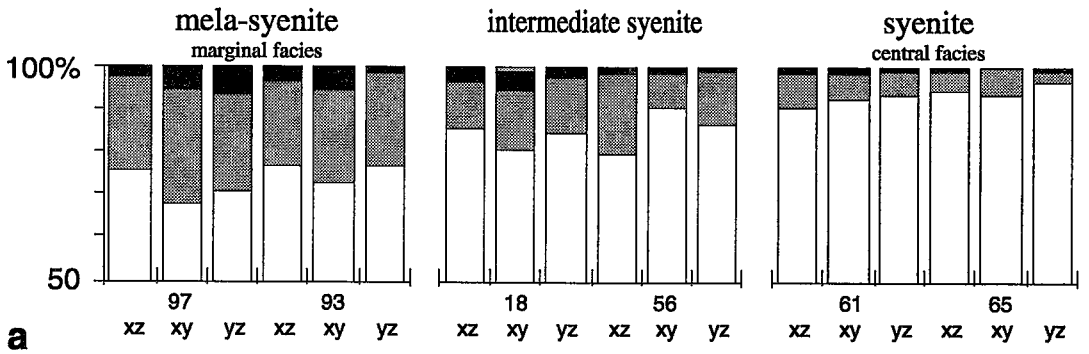

Modes

	average	σ	average	σ	average	σ
Titanite	0.1	*0.1*	0.4	*0.4*	0.2	*0.1*
Biotite+Mag.	4.9	*2.0*	2.9	*1.2*	1.3	*0.5*
Pyroxene	22.3	*2.2*	13.0	*3.7*	5.6	*1.2*
K-feldspar	72.7	*3.5*	83.7	*4.1*	92.9	*1.7*
	mela-syenite		inter.		syenite	

b

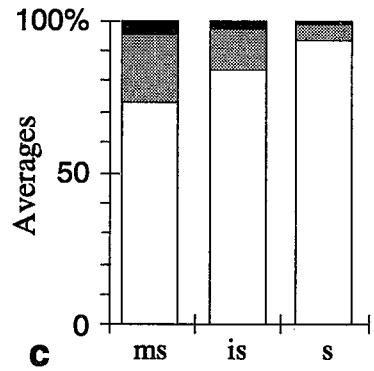

FIG. 5. Modes of K-feldspar, pyroxene, biotite + magnetite and titanite in the Lebel Stock. (a) Individual results showing the modal variations between facies and thin sections (oriented parallel to the principal axes of the magnetic fabric, x, y, z). (b) Averages and standard deviaitons between modes. (c) Average modes.

13% and 6% for the marginal, intermediate and central syenite units, respectively, and those of biotite + magnetite, 5%, 3% and 1%. Standard deviations of mineral modes, determined for each facies of the intrusion (Fig. 5b), indicate the degree of compositional heterogeneity between thin sections. Titanite, which constitutes 0.4% of the intermediate facies and 0.1% of the other facies, shows a large standard deviation because of its low mode and wide dispersion. The standard deviations of the other minerals are relatively small, and always less than the percentage differences between facies. The intermediate syenite shows the highest standard deviations in mineral modes, indicating a greater cm-scale compositional heterogeneity than the marginal or central facies. This may be due to incomplete mechanical mixing between mafic and felsic syenites, as suggested by Sutcliffe *et al.* (1990) for the origin of melasyenite in the petrologically similar Otto Stock, exposed 2 km southwest of the Lebel Stock. The subtle heterogeneities reported here would not have been detected using whole-rock geochemistry or mineral norms.

Mont-Louis – Andorra Pluton (digitized video camera images)

The *ca.* 300 Ma old Mont-Louis – Andorra Pluton is located in the Axial Zone of the Pyrénées, and intrudes Cambrian to Lower Carboniferous sediments (Autran *et al.* 1970, Pouget *et al.* 1989). It is normally zoned, from quartz diorite with numerous mafic enclaves at the margin, through granodiorite to monzonite in the core (Gleizes *et al.* 1993). A steep compositional gradient occurs between the monzonite and the granodiorite, whereas the transition between granodiorite and quartz diorite is gradational.

To differentiate between plagioclase, K-feldspar and quartz in these rocks, slabs cut parallel to the principal planes of the magnetic fabric ellipsoid and stained with sodium cobaltinitrite and red amaranth (Bailey & Stevens 1960, Laniz *et al.* 1964) were analyzed, although this did not allow the distinction between amphibole and biotite. Multichannel digital images were made with a monochrome CCD camera and color-pass filters (Appendix). PCA was not neces-

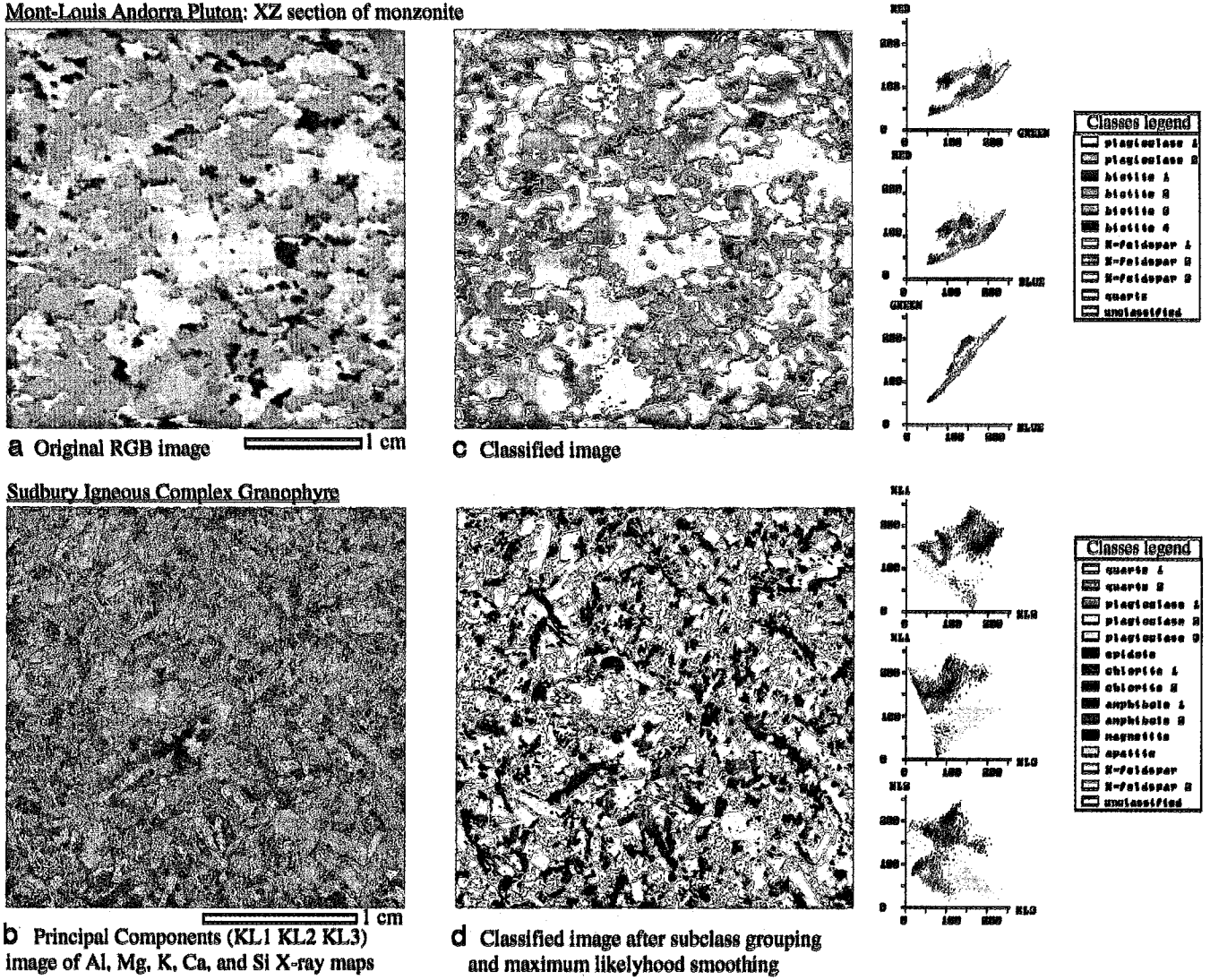

FIG. 6. (a) Original RGB image of a stained slab of monzonite from the Mont-Louis – Andorra Pluton, made with a black-and-white CCD video camera using three-color pass filters (see Appendix). (b) Classified image and scattergrams showing the definition of subclasses. (c) False-color composite image of the three first principal components of Al, Ca, Mg, K, and Si, X-ray map images of granophyre from the Sudbury Igneous Complex (KL1: Red, KL2: Green, and KL3: Blue). (d) Classified image after the grouping of subclasses and postclassification smoothing and scattergrams used for the classification.

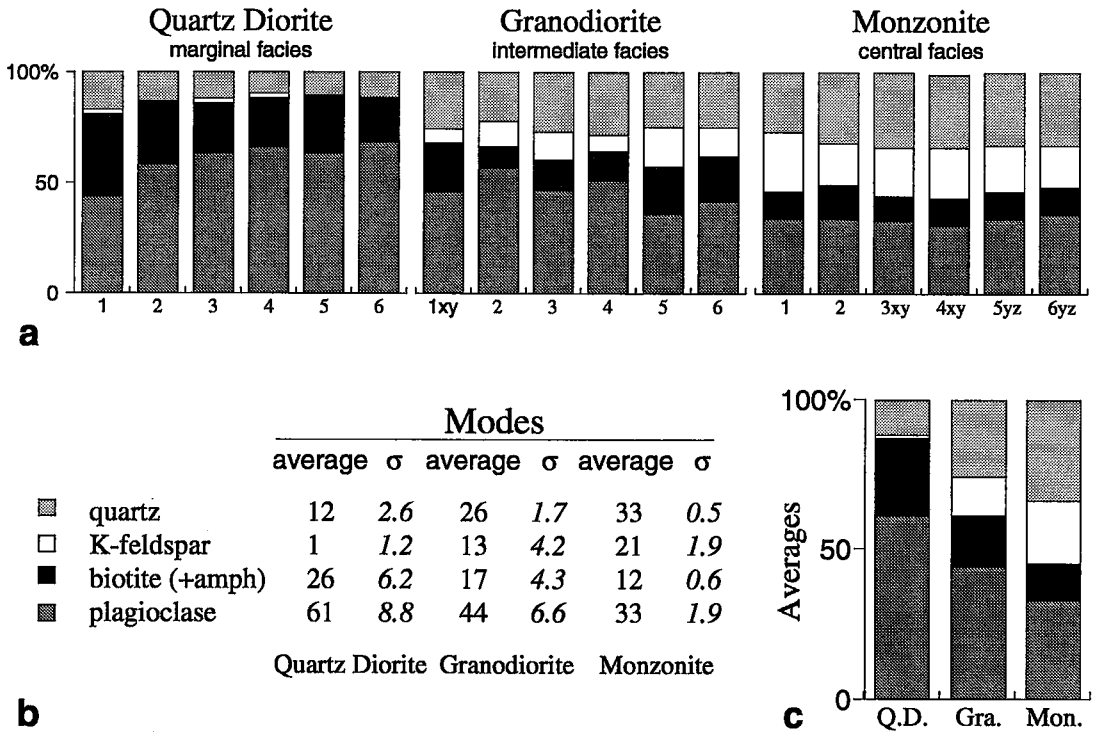

FIG. 7. Modes of plagioclase, biotite (± amphibole), K-feldspar and quartz in the Mont-Louis – Andorra pluton. (a) Individual results showing the modal variations between facies and slabs. (b) Averages and standard deviations between modes. (c) Average modes.

sary in this suite of samples because of the distinct colors of each phase (Fig. 6a). The modes, determined from counting areas *ca.* 12 cm^2 (96 000 pixels) of 18 samples analyzed from the three principal facies of the pluton, are presented in Figure 7.

Modes determined from the classified images (Fig. 6b) are similar to those reported in previous studies of the pluton (Autran *et al.* 1970, Gleizes *et al.* 1993), but because numerous and differently oriented sections were analyzed, several new observations on the modal variability of the pluton are evident (Fig. 7b). The standard deviations of all mineral modes are greater in the quartz diorite and granodiorite than in the monzonite. In the quartz diorite, the modal heterogeneity is due to clusters of mafic minerals which form irregular patches and schlieren. In the granodiorite, the largest deviations in mineral mode are due to the presence of irregular centimeter scale patches of K-feldspar with complex amoeboid boundaries. Quartz is markedly constant in all three facies. The very constant modes of the monzonite probably reflect a homogeneous distribution of minerals, as would be expected for crystallization in a closed system. By contrast, the strongly variable modes of the quartz diorite and granodiorite may be due to crystallization in a more dynamic environment, in which flow-related mechanical clustering, magma mixing, or melt migration could produce the observed cm-scale heterogeneities.

Granophyre from the Sudbury Igneous Complex (electron-microprobe X-ray element maps)

Modal analysis of a sample of granophyre from the North Range of the Sudbury Igneous Complex (Naldrett & Hewins 1984) is presented. This sample was difficult to analyze using electro-optical techniques because the feldspars and quartz could not be separated due to their similar grey-levels and fine granophyric intergrowth. Fine-grained products of alteration, such as epidote and chlorite, also lead to difficulties in the classification of the main mafic phases. Furthermore, because of the strong alteration, staining could not be successfully applied. Therefore, X-ray imaging using a microprobe seemed to be the most appropriate technique for the analysis of this rock.

Five elemental X-ray maps (Al, Ca, Mg, K, Si; 512 × 512 pixels), obtained from the center of a large polished thin section, were used for the analysis

(Appendix). Grey-levels in a single-channel elemental X-ray map represent the relative concentration of the element, normalized to 256 levels. Because of their unique chemistry, the ranges in grey-levels of most minerals define sharp peaks on the image histogram, with less overlap than those typical of electro-optical images (*viz.*, Fig. 3). Many mineral phases can therefore be successfully separated by thresholding the image histogram of a single-channel image. However, because no single element occurs in all different mineral species in unique amounts, a full recognition of all the phases in a single-channel image is rarely possible. We have found that the most effective approach for the classification of multichannel X-ray maps is to firstly decorrelate and concentrate the information using PCA (Fig. 6c), and secondly to perform a minimum distance to means multichannel classification on the first three principal-component images (Fig. 6d).

The effect of the KL transformation on the data is summarized in Tables 1 and 2. Prior to transformation, the information content (σ^2; Appendix) is evenly distributed throughout all five channels of the X-ray map (Table 1). Following the transformation, 88% of the information content is now concentrated within the first three components (λ; Table 2). The remaining 12% of the information, left in the KL4 and KL5 channels, largely corresponds to noise. The first three principal components can now be displayed as a pseudo-color image (Fig. 6c) in which each mineral is characterized by a distinct color. The chemical composition corresponding to each color can be checked by examining the original element-distribution maps. Information, not obvious in thin section or single-channel data, on the nature and spatial distribution of the alteration of minerals also can be determined, and is important for the definition of subclasses during classification of the image.

The KL1, KL2, KL3 pseudocolor image (Fig. 6c) was used for mineral identification (Fig. 6d) according to the training and classification procedures outlined previously. The number of pixels belonging to each subclass (Table 3, raw-data column) was determined from a 6.55-cm^2 (262 144 pixel) area. When grouping the subclasses, chlorite was included with amphibole because it almost always occurs as alteration-related inclusions in the amphibole. A statistical smoothing filter (Appendix) was applied to reduce the number of misclassified pixels in the classified image. This increased the number of unclassified pixels from 0.2 to 4.5% (Table 3, processed data column), and caused a slight change in the area of each phase due to the deletion of mixed pixels at grain boundaries (*e.g.*, Fig. 2b) and within-phase noise. For most minerals this change in area is less than or equal to 2%. The area of plagioclase increased by 2.2%, whereas that of epidote was reduced by 1.8% because of the replacement of some small epidote grains by plagioclase during application of the smoothing filter. Although this resulted in an underestimation in the mode of epidote, greater accuracy would have required a much higher spatial resolution. The same effect deleted a few needles of apatite, and magnetite lost 2.2% in area due to misidentification with certain amphibole grains that are intergrown with a Ca-rich alteration. The magnetite mode is considered accurate, as verified by comparison to the original thin section. The final mode (Table 3, mode column) is a good estimation of the composition of the rock at the 50-μm scale.

TABLE 1. CONTRAST IN THE X-RAY MAP IMAGE OF THE GRANOPHYRE

Channel i	Al	Ca	Mg	K	Si	C
σ^2_i	3320.5	925.1	2514.7	2051.7	2553.5	11365
C%	29.2	8.1	22.1	18.1	22.5	100

Channel i: major elements. σ^2_i: grey level standard deviations or contrast of the X-ray map channels. C: sum of σ^2_i, total contrast or amount of information in the image. C%: percentage of the total contrast in each channel.

TABLE 2. CONTRAST IN THE KL IMAGE OF THE GRANOPHYRE

Channel j	KL 1	KL 2	KL 3	KL 4	KL 5	C_{KL}
λ_j	4148.7	3880.2	1969.7	1123.6	243.3	11365
C_{KL}%	36.5	34.1	17.3	9.9	2.1	100

Channel j: principal components of the X-ray maps following principal components analysis. λ_j: eigenvalues of the covariance matrix of the X-ray map channels used for the Karhunen-Loéve (KL) transformation, and contrast of the new channels (KL1 to KL5). C_{KL}: sum of λ_i, or total contrast of the KL channels (equal to C in the original image) shows that all information is preserved.
C_{KL}%: percentage of total contrast in each channel. Note that most of the information is now concentrated in the first three channels (88% of C).

CONCLUSIONS

Multichannel classification, as developed for the analysis of digital multispectral satellite and aircraft images (Lillesand & Kiefer 1987), also can be applied to digital multichannel images of rocks at length scales between about five centimeters to less than one millimeter. Such images are made using electro-optical devices (scanners, CCD cameras), in which the image channels are the primary visible colors, or with an electron microprobe, as X-ray element maps. Although X-ray element mapping is time-consuming (0.1 s/pixel dwell-time *versus* 0.1 μs/pixel dwell-time for a CCD device; Appendix), it provides images with higher spatial resolution and greater ability to separate mineral phases than is usually possible with electro-optical images, in which only the rock-forming minerals can normally be identified. Problems related

TABLE 3. GRANOPHYRE CLASSIFICATION AND MODAL ANALYSIS DATA

Class names	*comments*	Raw Data			Processed Data		
		subclasses		classes	classes		**Modes**
	pixel size 50µm	pixels	%area	%area	pixels	%area	%
unclassified		496	0.2	0.2	11881	4.5	**0.0**
quartz 1		20863	8.0				
quartz 2	*with K-feld mixed on edges*	36747	14.0	22.0	56415	21.5	**22.5**
plagioclase 1		35676	13.6				
plagioclase 2	*rich in sericite*	12029	4.6				
plagioclase 3	*rich in epidote*	31021	11.8	30.0	84464	32.2	**33.8**
epidote	*free grains*	9083	3.5	3.5	4408	1.7	**1.8**
chlorite 1	*with sericite (K rich)?*	4595	1.8				
chlorite 2		8433	3.2	5.0			
amphibole 1	*with low alteration*	13777	5.3				
amphibole 2	*with chlorite + magnetite*	26665	10.2	15.4	52160	19.9	**20.8**
magnetite	*with other minerals*	14202	5.4	5.4	8280	3.2	**3.3**
apatite		2273	0.9	0.9	425	0.2	**0.2**
K-feldspar 1		19067	7.3				
K-feldspar 2	*with quartz mixed on edges*	27217	10.4	17.7	44111	16.8	**17.6**
sum		262144	100		262144	100	**100**

Raw Data : list of the number of pixels and percentages of each subclass counted after barycentric classification of the KL1, KL2, KL3 image; the percentages for each class are sums of the subclass counts. Processed Data : pixel counts and percentage for each class after subclass grouping and statistical smoothing of the resulting image. Modes (in bold text) are calculated for the number of classified pixels.

to finite size of pixels, mixed pixels and phase and phase-boundary definition still exist with both types of data. Choice of digitization technique should be made on the basis of the nature of the sample and the type of image-analysis measurements required.

Principal Component Analysis is used to decorrelate the information content of multichannel images, and allows for more effective visualization of differences in mineral colors. PCA is particularly useful for combining the large number of channels available in X-ray element maps. Minerals in the resulting pseudocolor image are well defined and easy to identify by comparing them to the original X-ray element images or thin section.

The success of any multichannel classification is dependent on the judgement and skill of the operator, because the mineralogy of the rock and the choice of training sites must be established by standard techniques of mineral identification prior to classification. When studying a suite of rocks of similar composition, the classification parameters need only be determined once. The procedures can therefore be used for rapid petrological measurements. The technique of modal analysis illustrated here is sufficiently precise to detect subtle heterogeneities in the modes of rock-forming minerals between samples digitized using electro-optical devices (Lebel Stock and Mont-Louis – Andorra pluton studies). A higher precision in determining modes can be achieved from X-ray element maps (Sudbury Igneous Complex granophyre).

ACKNOWLEDGEMENTS

PL acknowledges postdoctoral support from the Natural Sciences and Engineering Research Council of Canada (NSERC) and the Institut National des Sciences de l'Univers and Centre National de la Recherche Scientifique (URA n°67) for laboratory support during accomplishment of his Ph.D. thesis. ARC acknowledges the support of University of Toronto and NSERC Operating grants. We are grateful to Pierre-Yves Robin for many useful discussions on all aspects of this work. The X-ray element maps of the Sudbury Granophyre were kindly supplied by Jun Cowan (University of Toronto) under the supervision of John Rucklidge. The editorial comments of Frank Hawthorne led to a substantial improvement of the paper.

REFERENCES

AUTRAN, A., FONTEILLES, M. & GUITARD, G. (1970): Relations entre les intrusions de granitoïdes, l'anatexie et le métamorphisme général: cas de la chaîne hercynienne des Pyrénées orientales. *Bull. Soc. géol. France, Sér.* **7, XII**, 673-731.

BAILEY, E.H. & STEVENS, R.E. (1960): Selective staining of K feldspar and plagioclase on rock slabs and thin sections. *Am. Mineral.* **45**, 1020-1025.

CAMPBELL, J.B. (1987): *Introduction to Remote Sensing.* Guilford Press, New York.

CASHMAN, K.V. (1990): Textural constraints on the kinetics of crystallization of igneous rocks. *In* Modern Methods in Igneous Petrology: Understanding Magmatic Processes (J. Nicholls & J.K. Russell, eds.). *Rev. Mineral.* **24**, 259-314.

COSTER, M. & CHERMANT, J.L. (1990): *Précis d'analyse d'images.* Presse du CNRS, Paris.

CRUDEN, A.R. & LAUNEAU, P. (1994): Structure, magnetic fabric and emplacement of the Archean Lebel Stock, S.W. Abitibi Greenstone Belt. *J. Struct. Geol.* **16**, 677-691.

FABBRI, A.G. (1984): *Image Processing of Geological Data.* Van Nostrand Reinhold, New York.

GLEIZES, G., NÉDÉLEC, A., BOUCHEZ, J.-L., AUTRAN, A. & ROCHETTE, P. (1993): Magnetic susceptibility of the Mont-Louis – Andorra ilmenite-type granite (Pyrénées): a new tool for the petrographic characterization and regional mapping of zoned granite plutons. *J. Geophys. Res.* **98**, 4317-4331.

GUPTA, R.P. (1991): *Remote Sensing Geology.* Springer-Verlag, Berlin.

JÄHNE, B. (1991): *Digital Image Processing, Concepts, Algorithms and Scientific Applications.* Springer-Verlag, Berlin.

JOURLIN, M. (1987): Rôle du Laplacien sous-jacent dans le rehaussement de frontière. *J. Microsc. Spectrosc. Electron.* **12**, 89-93.

KHOSLA, R.P. (1992): From photons to bits. *Physics Today* **45**(12), 42-49.

LANIZ, R.V., STEVENS, R.E. & NORMAN, M.B. (1964): Staining of plagioclase feldspar and other minerals with F. D. and C. red no. 2. *U.S. Geol. Surv., Prof. Pap.* **501-B**, 152-153.

LAUNEAU, P. & BOUCHEZ, J.L. (1992): Mode et orientation préférentielle de forme des granites par analyse d'images numériques. *Bull. Soc. géol. France* **163**, 721-732.

———, ——— & BENN, K. (1990): Shape preferred orientation of object populations: automatic analysis of digitized images. *Tectonophysics* **180**, 201-211.

LILLESAND, T.M. & KIEFER, R.W. (1987): *Remote Sensing and Image Interpretation.* John Wiley & Sons, New York.

LOÉVE, M. (1955): *Probability Theory* (third ed.). D. Van Nostrand Co., Princeton, New Jersey.

NALDRETT, A.J. & HEWINS, R.H. (1984): The main mass of the Sudbury Igneous Complex. *In* The Geology and Ore Deposits of the Sudbury Structure (E.G. Pye, A.J. Naldrett & P.E. Giblin, eds.). *Ontario Geol. Surv., Spec. Vol.* **1**, 235-251.

POUGET, P., LAMOUROUX, C., DAHMANI, A., DEBAT, P., DRIOUCH, Y., MERCIER, A., SOULA, J.C. & VEZAT, R. (1989): Typologie et mode de mise en place des roches magmatiques dans les Pyrénées hercyniennes. *Geol. Rundschau* **78**, 537-554.

PRATT, W.K. (1978): *Digital Image Processing.* John Wiley & Sons, New York.

RIPLEY, B.D. (1988): *Statistical Inference for Spatial Processes.* Cambridge University Press, Cambridge, U.K.

RUSS, J. C. (1992): *The Image Processing Handbook.* CRC Press, Boca Raton, Florida.

SUTCLIFFE, R., SMITH, A.R., DOHERTY, W. & BARNETT, R.L. (1990): Mantle derivation of Archean amphibole-bearing granitoid and associated mafic rocks: evidence from the southern Superior Province, Canada. *Contrib. Mineral. Petrol.* **105**, 255-274.

WILKINSON, L., CRUDEN, A. & KROGH, T. (1993): Structure and timing of post-Timiskaming ductile deformation along the Larder Lake – Cadillac deformation zone in the Kirkland Lake area. *Geol. Soc. Am., Abstr. Programs* **25**, A-236.

Received August 9, 1993, revised manuscript accepted March 13, 1994.

APPENDIX

Creating digital images

Electro-optical devices. A Sony CCD (coupled charge device) video camera (sensing area: 8.8 × 6.6 mm) and a digitizing card were used for the study of the Mont-Louis – Andorra pluton, and an Abaton 24-bit flat-bed color scanner was used for the Lebel Stock study. A detailed description of the operation of both devices was given by Pratt (1978), Jähne (1991) and Khosla (1992). Both instruments record information on the intensity of incident visible electromagnetic radiation that is reflected or transmitted by the sample. The intensity of the signal produced by a CCD cell is a function of the number of photons that strike it over a given "dwell-time", which is usually on the order of 0.1 μs. Most CCD cameras are designed for broadcast television and produce images with a ¾ shape ratio, which imparts an anisotropy to the pixels of the digital image. This distortion should be corrected before processing the image. A second source of distortion of the image comes from the digitization of the analog output signal from the camera because the grid size of the CCD is different from the grid size of the digitized image (580 × 500 on the CCD *versus* 512 × 512 on the image). Such distortions can be avoided by using a CCD with square pixels and a proper frequency of digitization (Russ 1992). For multispectral classification, the three primary colors must be available on three independent channels. Pixels in each channel should also correspond to the same point on the sample. This can be done directly with a 3-CCD, or 3-chip, camera, or indirectly with a black and white CCD camera using different color filters. It cannot be done with a conventional, single-chip, color video camera because primary color pixels are offset, rendering channel superpositions impossible. The digitizing card used to "grab" the image from the CCD must be able to record at least 8 bits per pixel, giving 256 grey-levels. Twenty-four-bit flat-bed scanners are well suited for petrological purposes, as the image grid is square (no distortion), light intensity is homogeneous over the entire image, and the resulting three 8-bit channels (RGB) are ideal for multispectral analysis.

Microprobe device. A CAMECA SX–50 electron microprobe (Department of Geology, University of Toronto) was used to create X-ray maps of five major elements (Al, K, Mg, Ca, Si) for the study of the Sudbury Igneous Complex granophyre by mechanically translating a polished thin section beneath a stationary, 50-μm-wide defocused electron-beam. The stage was moved continuously in the row direction at a velocity determined by the 0.1 s "dwell-time", during which X rays are counted for each pixel, giving a beam path on the thin section of 50 μm per pixel. The distance between rows was set to 50 μm to produce a square grid between pixel centers.

Image processing

Images were processed using the software package DIDACTIM (ICARE International, Prologue – B.P. 2736, 31312 Babège Cedex, France) on a 486DX33 PC clone with a VIPIX RGB image-display card and Mitsubishi 20" RGB color monitor. Most commercial image-processing packages for remote sensing applications are capable of the main filtering and classification procedures recommended here. Certain routines (post-classification smoothing, modal and other analyses) must be programmed independently.

Preprocessing of the image is usually required before classification. This step must be global and linear in order to maintain the mutual relationships among pixels, and hence to safeguard information content. Among the many techniques that are available (Ripley 1988, Jähne 1991, Russ 1992), the following procedures were used for our images.

Blank-image correction. A blank image is generated in order to record noise coming from the CCD camera, such as dust on the lens and lighting variations. For each pixel, the calculated average grey-level of the digitized blank image is subtracted from the original blank image (Russ 1992). This difference is then subtracted from the image to be corrected.

Denoising filter. Random electronic noise with a high spatial frequency is removed using a low-pass filter (Pratt 1978). A digital filter, also known as a kernel or sliding mask, is an array of numerical values that is moved across the image, and centred consecutively on each pixel. The new pixel value is given by the sum of the products of the array values and the underlying pixel values. This value is usually normalized by the sum of the kernel coefficients in order to keep the final pixel value between 0 and 255. The matrix, A1, which calculates a weighted average of the nine neighboring pixel values (Pratt 1978), is particularly well suited for denoising electro-optical images.

$$\begin{matrix} 1 & 3 & 1 \\ 3 & 9 & 3 \\ 1 & 3 & 1 \end{matrix} \qquad \text{(A1)}$$

For example, application of this kernel on a pixel (x, y) gives the following intensity z_i for each channel i:

$$\begin{aligned} z_i(x, y) = & \\ & \{1\, z_i(x-1, y-1) + 3\, z_i(x, y-1) + 1\, z_i(x+1, y-1) \\ & 3\, z_i(x-1, y) + 9\, z_i(x, y) + 3\, z_i(x+1, y) \\ & 1\, z_i(x-1, y+1) + 3\, z_i(x, y+1) + 1\, z_i(x+1, y+1)\} /25 \end{aligned}$$

Sharpening filter. The hazy image produced during denoising can be sharpened by adding a fraction of the Laplacian of the image to the image (Jourlin 1987,

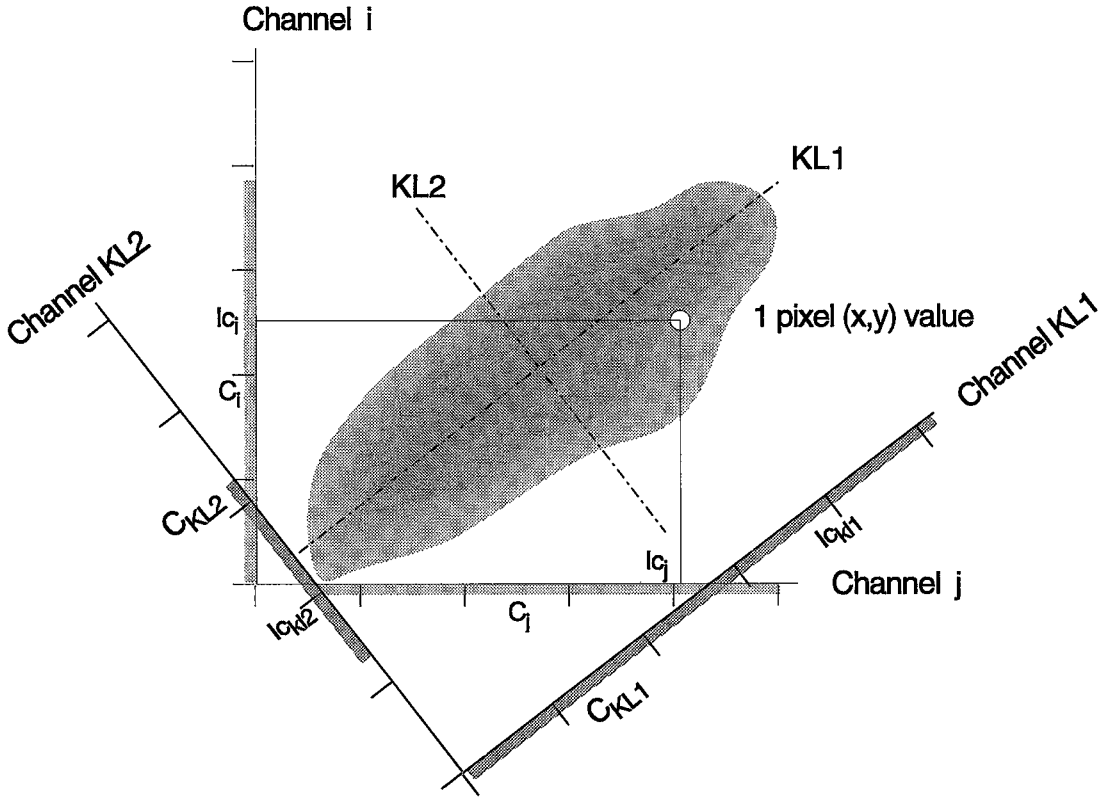

FIG. A1. Illustration of a Principal Component Analysis (PCA) or Karhunen – Loéve (KL) transformation of channels i and j. The first component (KL1 is given by the direction of maximum contrast in the image. The second (KL2) is the maximum contrast orthogonal to KL1. After transformation, a pixel located in column x and row y, with intensities Ic_i and Ic_j, becomes Ic_1 and Ic_2 in the new KL1, KL2 system of coordinates. C_i and C_j are the original contrasts, and C_{kl1} and C_{kl2} are the contrasts after KL transformation.

Russ 1992). Matrix A2 is used for this purpose (Launeau *et al.* 1990) and is also useful for enhancing edges between phases.

$$\begin{matrix} -1 & -4 & -1 \\ -4 & 30 & -4 \\ -1 & -4 & -1 \end{matrix} \qquad \text{(A2)}$$

Principal Component Analysis (PCA). For images of very low contrast, the Karhunen–Loéve transformation (Loéve 1955) or PCA is used to decorrelate the information in each channel (Lillesand & Kiefer 1987). It can also be used to concentrate the information carried by many channels. The covariance matrix Q of three or more channels is calculated using equation A3. If $Ic_i(x,y)$ and $Ic_j(x,y)$ are the intensities of the pixel (x,y) in the channels c_i and c_j, and Nx, Ny are the number of columns and rows, then the covariance of the channels is:

$$\text{COV}(ci, cj) = \frac{1}{\text{Nx.Ny}} \sum_{y=1}^{Ny} \sum_{x=1}^{Nx} (Ic_i(x,y)-\overline{Ic_i})\,(Ic_j(x,y)-\overline{Ic_j}) \qquad \text{(A3)}$$

where $\overline{Ic_i} = \frac{1}{\text{Nx.Ny}} \sum_{y=1}^{Ny} \sum_{x=1}^{Nx} Ic_i(x,y)$

For an RGB image, the covariance matrix of the image is:

$$Q = \begin{bmatrix} \text{COV}(c_R,c_R) & \text{COV}(c_R,c_G) & \text{COV}(c_R,c_B) \\ \text{COV}(c_G,c_R) & \text{COV}(c_G,c_G) & \text{COV}(c_G,c_B) \\ \text{COV}(c_B,c_R) & \text{COV}(c_B,c_G) & \text{COV}(c_B,c_B) \end{bmatrix} \qquad \text{(A4)}$$

The covariance of one channel with respect to itself is equal to its standard deviation, σ^2, and is a measure of the contrast, or information content of the channel:

$$\mathrm{COV}(ci, ci) = \frac{1}{Nx.Ny}\sum_{y=1}^{Ny}\sum_{x=1}^{Nx}(Ic_i(x,y)-\overline{Ic_i})^2 = \sigma^2(c_i) \quad \text{(A5)}$$

The sum of the diagonal components of Q gives the total contrast C,

$$C = \sigma^2(c_R) + \sigma^2(c_G) + \sigma^2(c_B) \quad \text{(A6)}$$

The goal of the Karhunen–Loéve (KL) transformation is to determine the direction of maximum contrast in the channel space of the image (Fig. A1). This operation defines a new axis oriented in the long dimension of the distribution of the data. Projection of the data onto this axis gives a new set of intensity values in the "first component" channel (KL1). Similarly, the "second component" (KL2) is calculated to find the second axis perpendicular to KL1 (Fig. A1). The "third component" (KL3) is perpendicular to KL1 and KL2. Collectively, KL1,2,3 are known as the principal component axes. Their directions are given by the eigenvectors of the covariance matrix, and their intensities by the eigenvalues λ_i:

$$Q_{KL} = \begin{bmatrix} \lambda_2 & & \\ & \lambda_1 & \\ & & \lambda_3 \end{bmatrix} \text{ with } (\lambda_1 > \lambda_2 > \lambda_3) \quad \text{(A7)}$$

This operation is equivalent to a rotation of the axes of the coordinate system (Fig. A1), and the sum of the eigenvalues of the matrices Q and Q_{KL} is constant. All of the contrast or information is preserved during the KL transformation, and $C = C_{KL} = \lambda_1 + \lambda_2 + \lambda_3$. If the corresponding eigenvectors of Q are:

$$KL1 = \begin{bmatrix} c_{1R} \\ c_{1G} \\ c_{1B} \end{bmatrix} \quad KL2 = \begin{bmatrix} c_{2R} \\ c_{2G} \\ c_{2B} \end{bmatrix} \quad KL3 = \begin{bmatrix} c_{3R} \\ c_{3G} \\ c_{3B} \end{bmatrix}$$

then the KL transformation is

$$\begin{aligned} I_{KL1}(x,y) &= c_{1R}\, Ic_R(x,y) + c_{1G}\, Ic_G(x,y) + c_{1B}\, Ic_B(x,y) \\ I_{KL2}(x,y) &= c_{2R}\, Ic_R(x,y) + c_{2G}\, Ic_G(x,y) + c_{2B}\, Ic_B(x,y) \\ I_{KL3}(x,y) &= c_{3R}\, Ic_R(x,y) + c_{3G}\, Ic_G(x,y) + c_{3B}\, Ic_B(x,y) \end{aligned} \quad \text{(A8)}$$

and the new channels of the transformed image are called KL1, KL2 and KL3. The new intensities of each KL channel must be normalized to the maximum intensity of KL1 because the original length of KL1 can be greater than 255 (there are 360 possible intensity values for an axis inclined at 45° between channels i and j).

Post-classification smoothing

The values of pixels in the classified image are now used as labels, describing the mineral subclasses, as opposed to the quantities of the original image. Spatial filters, used in the preprocessing stage, can no longer be applied to smooth the salt-and-pepper appearance of the image because post-classification smoothing algorithms must operate on the basis of logical operations, rather than simple arithmetic computations (Lillesand & Kiefer 1987). Smoothing is done using various "majority filters". An example of such a routine, which was developed for smoothing classified X-ray map images, follows. First, a search is made for pixels that have two neighbors or less than two neighbors belonging to the same class. Then, using the kernel, A9, and the algorithm below:

$$\begin{array}{ccccc} & 1 & 2 & 1 & \\ 1 & 3 & 4 & 3 & 1 \\ 2 & 4 & 8 & 4 & 2 \\ 1 & 3 & 4 & 3 & 1 \\ & 1 & 2 & 1 & \end{array} \quad \text{(A9)}$$

"for each phase, i, of the kernel, $P_i = \Sigma$ {if $\mathrm{pixel}_{x,y}$ ε class i : 1 else 0} $\times$ C_{xy}" the number of pixels belonging to each phase weighted by the corresponding coefficients is calculated. The central pixel is then assigned to the majority class except where two classes are equally represented, or where the weighted density of the majority class is less than 16, in which case the pixel is not classified. A weighted density-limit of 16 is chosen; below this value, there is insufficient statistical representation of any class in the area surrounding the pixel in question.